https://doi.org/10.2352/EI.2026.38.15.COIMG-123

Fixed-Basis Low-Rank Tensor Approximation for the Fusion of Hyperspectral and Multispectral Imagery

James E. Fowler
Mississippi State University, Starkville, MS USA
Email: fowler@ece.msstate.edu

Abstract

The inverse-imaging problem comprising the fusing of a hyperspectral image, possessing high spectral resolution, with a multispectral image, having high spatial resolution, to yield an image with high resolution both spatially and spectrally is considered. In particular, a prior state-of-the-art approach—low-rank tensor approximation (LRTA)—is revisited with the goal of simplifying its implementation and accelerating its execution speed. Whereas the original LRTA incorporated low-rank objectives both spatially and spectrally, the revised algorithm employs spectral low-rankness exclusively. Additionally, the reliance of LRTA on singular value thresholding (SVT)—an operator widely used to impose low-rankness in optimizations—is replaced with a fixed-basis approximation that eliminates the computationally costly singular value decomposition required by the SVT. The proposed modifications ultimately result in significant runtime speedup; furthermore, empirical results reveal improved fusion quality when compared to the original LRTA.

Introduction

Many remote-sensing applications are driven by either multispectral imagery (MSI) acquired at high spatial resolution but relatively low spectral resolution, or hyperspectral imagery (HSI) which, in contrast, has high spectral resolution but low spatial resolution. Many of these applications would benefit if an image with both high spectral and spatial resolution—which we call HS^{2}I—were available; yet, due to an inevitable tradeoff between spatial and spectral resolution, acquiring such an HS^{2}I directly with optical remote-sensing systems is generally impossible. This has led to increasing interest in hyperspectral-multispectral (HS-MS) fusion [1], which can be considered to be a form of inverse imaging in which two sets of measurements—the HSI and the MSI—are fused together to recover the unknown target HS^{2}I. Past literature includes numerous techniques for solving the HS-MS fusion problem, including classic matrix-based [2, 3] and tensor-based [4, 5] approaches, as well as traditional proximal optimization [6] common to inverse-imaging solutions.

In particular, [7] introduced a method called low-rank tensor approximation (LRTA) which was formulated mathematically as a convex optimization of a tensor trace norm imposing low rank spatially as well as spectrally. Whereas prior tensor-based fusion approaches (e.g., [8, 9]) typically resorted to a tensor decomposition, in contrast, LRTA exploited ideas from the field of tensor completion to directly impose a low-rank property spatially and spectrally while avoiding the computationally complex patch clustering and dictionary learning common to competing techniques based on tensor decomposition. Experimental results reported in [7] demonstrated that LRTA provided highly effective fusion preserving both spatial details and texture while yielding significantly improved image quality when compared to other state-of-the-art HS-MS fusion methods.

In this paper, we revisit LRTA with a goal of simplifying its implementation and accelerating its execution speed. To do so, we explore two revisions to the LRTA algorithm. Since it is common for an HS^{2}I to have spectral rank that is much lower than spatial rank, LRTA often experiences a diminished contribution from the spatial-rank component of its optimization in practice. Consequently, the first proposed modification eliminates consideration of spatial rank, refocusing the algorithm on spectral rank exclusively. Additionally, as is common with low-rank optimizations, LRTA relies on singular value thresholding (SVT) [10], which, in turn, requires the computation of a singular value decomposition (SVD). Yet, the SVD is notorious for its computational complexity as well as for being difficult to implement on GPUs efficiently and stably. Thus, as a second revision to LRTA, we introduce what we call a fixed-basis SVT (FB-SVT) that eliminates dependence on the computationally costly SVD in favor of a fast approximation to it. We call the resulting revised algorithm the fixed-basis LRTA (FB-LRTA), and we find experimentally that the proposed FB-LRTA offers not only significant computational speedup over the original LRTA, but also increased image quality in the HS-MS fusion task.

Below we develop our proposed FB-LRTA algorithm in detail. We start first with some mathematical preliminaries, following with a description of the proposed FB-SVT approximation to the SVT. We then briefly overview the original LRTA algorithm before presenting the proposed FB-LRTA variant driven by the FB-SVT. We conclude with experimental results conducted on a collection of imagery.

Preliminaries

Let real-valued, three-way tensor $\mathscr{X} \in \mathbb{R}^{M\times N\times C}$ have M rows, N columns, and C spectral bands. This tensor may be unfolded along mode 3 to produce a matrix, $\mathscr{X}_{(3)} \triangleq \text{unfold}_3(\mathscr{X}) \in \mathbb{R}^{C\times MN}$; unfolding along modes 1 and 2 is defined similarly (see, e.g., [7]). We use a trace norm as a convex proxy for tensor rank, specifically adopting the trace norm from [11],

$$\left\|\mathscr{X}\right\|_* \triangleq \sum_{k=1}^{n} \alpha_k \left\|\mathscr{X}_{(k)}\right\|_*, \tag{1}$$

where $\left\|\cdot\right\|_*$ is the matrix nuclear norm, and $\alpha_k \geq 0$ are weights such that $\sum_{k=1}^{n} \alpha_k = 1$. We also define the Frobenius norm of a tensor as $\left\|\mathscr{X}\right\|_F \triangleq \left\|\mathscr{X}_{(k)}\right\|_F$ which holds

for any k. For N-dimensional vector $\mathbf{x} = \begin{bmatrix} x_1 & \cdots & x_N \end{bmatrix} \in \mathbb{R}^N$, let $\sqrt{\mathbf{x}}$ denote the element-wise square root, i.e., $\sqrt{\mathbf{x}} \triangleq \begin{bmatrix} \sqrt{x_1} & \cdots & \sqrt{x_N} \end{bmatrix}$. Similarly, let the element-wise division of N-dimensional vectors be $\frac{\mathbf{x}}{\mathbf{y}} \triangleq \begin{bmatrix} \frac{x_1}{y_1} & \cdots & \frac{x_N}{y_N} \end{bmatrix}$. Finally, the spatial-interpolation operation of tensor $\mathscr{X}$ by ratio R is defined by $\mathscr{Z} = \text{interpolation}(\mathscr{X}, R, \text{“method”})$, which returns a tensor in which the two spatial orders are resized, i.e., $\mathscr{Z} \in \mathbb{R}^{RM \times RN \times C}$. Here, “method” indicates the interpolation process used, such bicubic interpolation.

The FB-SVT

Optimizations involving nuclear norms applied as a convex proxy for rank commonly involve the SVT in their solutions; see, e.g., [10]. The SVT operator is defined in [10] as

$$\text{svt}_\sigma(\mathbf{X}) \triangleq \mathbf{U}\,\text{shrink}_\sigma(\Sigma)\mathbf{V}^T, \tag{2}$$

where $\mathbf{X} = \mathbf{U}\Sigma\mathbf{V}^T$ is an SVD of matrix $\mathbf{X}$, and the matrix-valued shrinkage operator $\text{shrink}_\sigma(\mathbf{X})$ is the scalar shrinkage operator $\text{shrink}_\sigma(x) \triangleq \text{sgn}(x)\max\{|x| - \sigma, 0\}$ applied to each element of $\mathbf{X}$.

The primary issue with the SVT, particularly when employed in iterative solution procedures, is that it involves the calculation of an SVD every time the SVT is applied, and the SVD is costly from a computational perspective. Here, we propose an alternative—called the FB-SVT—that avoids the SVD and its associated computational burden. The FB-SVT operates similarly to the SVT, except that we assume that we already know the left eigenvectors $\mathbf{U}$ of $\mathbf{X}$ and so can dispense with the SVD calculation. Additionally, we eliminate dependence on $\mathbf{V}$ by employing the fact that, if the SVD of matrix $\mathbf{X}$ is $\mathbf{X} = \mathbf{U}\Sigma\mathbf{V}^T$, then the SVD of $\mathbf{X}\mathbf{X}^T$ is $\mathbf{X}\mathbf{X}^T = \mathbf{U}\Sigma^2\mathbf{U}^T$ since both $\mathbf{U}$ and $\mathbf{V}$ are unitary.[1] Thus, we define the FB-SVT as

$$\text{fb\_svt}_\sigma(\mathbf{X}, \mathbf{U}) \triangleq \mathbf{U}\,\text{diag}\left(\frac{\hat{\mathbf{d}}_\sigma(\mathbf{X}, \mathbf{U})}{\mathbf{d}(\mathbf{X}, \mathbf{U})}\right)\mathbf{U}^T\mathbf{X}, \tag{3}$$

where $\hat{\mathbf{d}}_\sigma(\cdot,\cdot)$ is scalar shrinkage applied to the diagonal vector of eigenvalues[2],

$$\hat{\mathbf{d}}_\sigma(\mathbf{X}, \mathbf{U}) \triangleq \text{shrink}_\sigma\Big(\mathbf{d}(\mathbf{X}, \mathbf{U})\Big), \tag{4}$$

and

$$\mathbf{d}(\mathbf{X}, \mathbf{U}) \triangleq \sqrt{\text{diag}\,(\mathbf{U}^T\mathbf{X}\mathbf{X}^T\mathbf{U})}. \tag{5}$$

The diagonal of $\mathbf{U}^T\mathbf{X}\mathbf{X}^T\mathbf{U}$ is the vector of the squares of the eigenvalues of $\mathbf{X}$, permitting the FB-SVT to avoid having to calculate an SVD as is required for the traditional SVT; however, the drawback is that the left eigenvectors $\mathbf{U}$ must be known *a priori*. We will return to the issue of how we arrive at $\mathbf{U}$ in the context of the FB-LRTA algorithm below.

[1] We are motivated to eliminate $\mathbf{V}$ because, if $\mathbf{X} = \mathscr{X}_{(3)} \in \mathbb{R}^{C \times MN}$ with $MN \gg C$ (i.e., the number of pixels in an HS^{2}I is much larger than the number of spectral bands), then $\mathbf{V} \in \mathbb{R}^{MN \times C}$ is much larger in size than $\mathbf{U} \in \mathbb{R}^{C \times C}$. Thus, using $\mathbf{U}$ alone is less computationally expensive and more memory efficient.

[2] Here, the $\text{diag}(\cdot)$ operator extracts the main diagonal as a vector when passed a matrix, or conversely constructs a diagonal matrix when passed a vector.

The Original LRTA Algorithm

The original LRTA algorithm [7] was designed to solve the HS-MS fusion problem when posed as follows. Assuming an unknown ground-truth HS^{2}I image $\mathscr{X} \in \mathbb{R}^{M \times N \times C}$, the observed HSI $\mathscr{L} \in \mathbb{R}^{M' \times N' \times C}$ and the observed MSI $\mathscr{H} \in \mathbb{R}^{M \times N \times C'}$ are produced as spatial and spectral degradations of the form

$$\mathscr{L}_{(3)} = \mathscr{X}_{(3)}\mathbf{D}, \tag{6}$$

$$\mathscr{H}_{(3)} = \mathbf{S}\mathscr{X}_{(3)}, \tag{7}$$

where $M' < M$, $N' < N$, and $C' < C$. Here, $\mathbf{S} \in \mathbb{R}^{C' \times C}$ and $\mathbf{D} \in \mathbb{R}^{MN \times M'N'}$ constitute spectral-degradation and spatial-degradation processes, respectively. The HS-MS fusion task is then to produce an estimate $\hat{\mathscr{X}}$ of the HS^{2}I $\mathscr{X}$ from the observed HSI $\mathscr{L}$ and MSI $\mathscr{H}$.

LRTA is predicated on the expectation that the HS^{2}I exhibits strong correlations in spectrally adjacent bands as well as high similarity between spatially neighboring pixels, with both manifesting mathematically as low-rankness. Thus, LRTA solves

$$\begin{aligned} &\min_{\mathscr{X}} \sum_{k=1}^{3} \alpha_k \left\| \mathscr{X}_{(k)} \right\|_* \\ &\text{s.t.} \quad \mathscr{X}_{(3)}\mathbf{D} = \mathscr{L}_{(3)} \text{ and } \mathbf{S}\mathscr{X}_{(3)} = \mathscr{H}_{(3)}, \end{aligned} \tag{8}$$

where parameters α_k control the intensity of low-rank constraints on each mode of the expected fusion result.

The LRTA algorithm results from solving (8) via linearized alternating direction method of multipliers with adaptive penalty (LADMAP) [12–14], a variant of the widely-used alternating direction method of multipliers (ADMM) that is useful for when constituent subproblems do not have closed-form solutions, as is the case for (8). Specifically, [7] introduces auxiliary variables $\mathbf{M}_k$ for $\mathscr{X}_{(k)}$ for $k \in \{1,2,3\}$; Lagrange multipliers $\mathbf{Y}_1'$, $\mathbf{Y}_2'$, $\mathbf{Y}_k$; and penalty parameters μ, γ, and β. This results in the augmented Lagrangian

$$\begin{aligned} &\mathrm{L}_{\mu,\beta,\gamma}(\mathscr{X}, \mathbf{M}_1, \mathbf{M}_2, \mathbf{M}_3, \mathbf{Y}_1, \mathbf{Y}_2, \mathbf{Y}_3, \mathbf{Y}_1', \mathbf{Y}_2') = \\ &\sum_{k=1}^{3} \alpha_k \left\| \mathbf{M}_k \right\|_* + \sum_{k=1}^{3} \left\langle \mathbf{Y}_k, \mathscr{X}_{(k)} - \mathbf{M}_k \right\rangle + \\ &\left\langle \mathbf{Y}_1', \mathbf{M}_3\mathbf{D} - \mathscr{L}_{(3)} \right\rangle + \left\langle \mathbf{Y}_2', \mathbf{S}\mathbf{M}_3 - \mathscr{H}_{(3)} \right\rangle \\ &+ \frac{\mu}{2} \sum_{k=1}^{3} \left\| \mathscr{X}_{(k)} - \mathbf{M}_k \right\|_{\mathrm{F}}^2 + \frac{\beta}{2} \left\| \mathbf{M}_3\mathbf{D} - \mathscr{L}_{(3)} \right\|_{\mathrm{F}}^2 + \\ &\qquad \frac{\gamma}{2} \left\| \mathbf{S}\mathbf{M}_3 - \mathscr{H}_{(3)} \right\|_{\mathrm{F}}^2. \end{aligned} \tag{9}$$

Optimization problem (8) is then solved iteratively via LADMAP applied to (9), resulting in the final LRTA algorithm as depicted in Alg. 1. The complete derivation of Alg. 1, as well as the constituent equations implementing the various updates in steps 6–9, can be found in [7]. We note that both steps 6 and 7 in Alg. 1 require SVTs, and thus the associated SVDs constitute a bulk of the computation required for LRTA.

The Proposed FB-LRTA Variant

FB-LRTA is proposed primarily to simplify and speed up the original LRTA of [7]. The proposed simplifications take several

Algorithm 1 The Original LRTA Algorithm from [7]

Input: HSI $\mathscr{L}$, MSI $\mathscr{H}$, spatial degradation $\mathbf{D}$, spectral degradation $\mathbf{S}$; parameters α_k, μ, β, γ, $T_{\max}$;
Initialization: $\mathbf{Y}'_{1,0} = \mathbf{Y}'_{2,0} = \mathbf{Y}_{k,0} = \mathbf{0}$, $k \in \{1,2,3\}$; $\eta_1 = 10^{-4}$, $\eta_2 = 10^{-5}$; $t = 0$;
$\mathscr{X}_t = \text{interpolation}(\mathscr{L}, R, \text{“bicubic”})$;
$M_{k,t} = \text{unfold}_k\left(\mathscr{X}_t\right)$ for $k \in \{1,2,3\}$;
repeat
  update $\mathbf{M}_{k,t+1}$ via (8) of [7] for $k = 1,2$;
  update $\mathbf{M}_{3,t+1}$ via (17) of [7];
  update $\mathscr{X}_{t+1}$ via (21) of [7];
  update Lagrange multipliers $\mathbf{Y}_{k,t+1}$, $\mathbf{Y}'_{1,t+1}$ and $\mathbf{Y}'_{2,t+1}$ via (22), (23), and (24) of [7];
  $t \leftarrow t+1$;
until $\max\left(\left\|\mathbf{M}_{3,t}\mathbf{D} - \mathscr{L}_{(3)}\right\|_{\mathrm{F}}, \left\|\mathbf{S}\mathbf{M}_{3,t} - \mathscr{H}_{(3)}\right\|_{\mathrm{F}}\right) < \eta_1$ **and** $\left\|\mathscr{X}_t - \mathscr{X}_{t-1}\right\|_F < \eta_2$ **or** $t > T_{\max}$;
return $\mathscr{X} = \mathscr{X}_t$.

Algorithm 2 The FB-LRTA Algorithm

Input: HSI $\mathscr{L}$, MSI $\mathscr{H}$, spatial degradation $\mathbf{D}$, spectral degradation $\mathbf{S}$; parameters β, γ, $T_{\max}$;
Initialization: $\Lambda_1 = \Lambda_2 = \mathbf{0}$, $t = 0$;
$\mathbf{U}, \Sigma, \mathbf{V} = \text{SVD}\left(\mathscr{L}_{(3)}\right)$;
$\mathscr{X} = \text{interpolation}(\mathscr{L}, R, \text{“bicubic”})$;
for $t = 1, \ldots, T_{\max}$ **do**
  update $\mathscr{X}_{(3)}$ via (12);
  update Lagrange multipliers Λ_1 and Λ_2 via (13) and (14);
end for
return $\mathscr{X}$.

forms. First, FB-LRTA uses only the mode-3 nuclear norm in the optimization objective; i.e., (8) is revised to

$$\begin{aligned} &\min_{\mathscr{X}} \left\|\mathscr{X}_{(3)}\right\|_* \\ &\text{s.t.} \quad \mathscr{X}_{(3)}\mathbf{D} = \mathscr{L}_{(3)} \text{ and } \mathbf{S}\mathscr{X}_{(3)} = \mathscr{H}_{(3)}. \end{aligned} \tag{10}$$

This simplification is motivated by the fact that the mode-1 and mode-2 norms ended up with diminished contributions to the optimization in the experimental results reported in [7], since α_1 and α_2 were empirically optimized there to be on the order of 0.01 while α_3 was set to approximately 0.97 (see (30) of [7]). With this simplification, the need for auxiliary variables $\mathbf{M}_k$ and Lagrangian multipliers $\mathbf{Y}_k$ is eliminated, along with parameters α_k and μ. Thus, the augmented Lagrangian in (9) is simplified to

$$\begin{aligned} &\mathrm{L}_{\beta,\gamma}(\mathscr{X}, \Lambda_1, \Lambda_2) = \\ &\left\|\mathscr{X}_{(3)}\right\|_* + \left\langle \Lambda_1, \mathscr{X}_{(3)}\mathbf{D} - \mathscr{L}_{(3)} \right\rangle + \left\langle \Lambda_2, \mathbf{S}\mathscr{X}_{(3)} - \mathscr{H}_{(3)} \right\rangle + \\ &\qquad \frac{\beta}{2}\left\|\mathscr{X}_{(3)}\mathbf{D} - \mathscr{L}_{(3)}\right\|_{\mathrm{F}}^2 + \frac{\gamma}{2}\left\|\mathbf{S}\mathscr{X}_{(3)} - \mathscr{H}_{(3)}\right\|_{\mathrm{F}}^2, \end{aligned} \tag{11}$$

and Alg. 1 simplifies to Alg. 2.

At the heart of the iterative processing, LRTA step 7 in Alg. 1 is simplified to FB-LRTA step 6 in Alg. 2, while LRTA steps 6 and 8 in Alg. 1 are eliminated. Thus, three SVT operators in LRTA (steps 6 and 7) are replaced by one FB-SVT operator in FB-LRTA (step 6), resulting in significant speedup.

The FB-LRTA updates (steps 6 and 7 in Alg. 2) are derived from LADMAP applied to (11). Since these derivations closely follow those in [7] (albeit significantly simplified), in the interest of brevity, we present only the resulting update equations here.

Specifically, the update in step 6 of Alg. 2 involves $\mathscr{X}$ being updated in mode 3, but, rather than use an SVT as in LRTA, we apply the FB-SVT as previously discussed to reduce computation. Thus,

$$\begin{aligned} \mathscr{X}_{(3)} \leftarrow \text{fb\_svt}_{\frac{1}{\tau}} \Bigg(&\mathscr{X}_{(3)} - \frac{\beta}{\tau}\left[\mathscr{X}_{(3)}\mathbf{D} - \mathscr{L}_{(3)} + \frac{\Lambda_1}{\beta}\right]\mathbf{D}^T \\ &- \frac{\gamma}{\tau}\mathbf{S}^T\left[\mathbf{S}\mathscr{X}_{(3)} - \mathscr{H}_{(3)} + \frac{\Lambda_2}{\gamma}\right], \mathbf{U}\Bigg), \end{aligned} \tag{12}$$

where $\text{fb\_svt}_\sigma(\cdot,\cdot)$ is the FB-SVT defined above in (3)–(5). We note that the original LRTA requires an SVT calculation—and hence an SVD—for every iteration of step 7 in Alg. 1, while FB-LRTA avoids iterative calculation of the SVD entirely through use of the FB-SVT. Consequently, FB-LRTA can run significantly faster than LRTA.

FB-LRTA estimates the left eigenvectors $\mathbf{U}$ by performing a single SVD on the HSI $\mathscr{L}$ (step 3 of Alg. 2) prior to the start of the FB-LRTA iterations. In doing so, we effectively assume that we can well approximate the true eigenvector matrix of the unknown target HS^{2}I $\mathscr{X}_{(3)}$ with the eigenvectors of the known HSI $\mathscr{L}_{(3)}$. We argue that this is possible since the eigenvectors of the HS^{2}I $\mathscr{X}_{(3)}$ essentially span the space of the constituent spectral signatures of the materials in the scene being imaged, and, since $\mathscr{L}_{(3)}$ is simply the same scene with a lower spatial resolution (but the same spectral resolution), its eigenvectors should span very nearly the same spectral space. We note a similar effect has been observed in the approximate invariance of the spectral eigendecomposition to spatial subsampling of hyperspectral imagery [15].

To finish our description of FB-LRTA, we conclude with the updating of the Lagrange multipliers Λ_1 and Λ_2 in step 7 of Alg. 2:

$$\Lambda_1 \leftarrow \Lambda_1 + \beta\left(\mathscr{X}_{(3)}\mathbf{D} - \mathscr{L}_{(3)}\right), \tag{13}$$

$$\Lambda_2 \leftarrow \Lambda_2 + \gamma\left(\mathbf{S}\mathscr{X}_{(3)} - \mathscr{H}_{(3)}\right). \tag{14}$$

These updates follow directly from the corresponding updates in LRTA step 9 in Alg. 1 which are derived in detail in [7], so we do not duplicate the derivations here.

Experimental Results

To gauge performance, we consider eight datasets as depicted in Fig. 1: the well-known Pavia University, Chikusei, DC Mall, Salinas, and Cuprite images, as well as a bespoke collection of images over the city of Los Angeles. In each case, the Wald protocol [16] is invoked, treating the original HSI as the target HS^{2}I $\mathscr{X}$ and applying spatial and spectral degradation operators, $\mathbf{D}$ and $\mathbf{S}$, respectively, to artificially generate HSI $\mathscr{L}$ and MSI $\mathscr{H}$ via (6) and (7), respectively. This permits using peak signal-to-noise ratio (PSNR) as a full-reference image-quality measure to quantitatively gauge performance.

The Pavia University image[3] was acquired by a Reflective Optics System Imaging Spectrometer (ROSIS) sensor over

[3] http://www.ehu.eus/ccwintco/index.php?title=Hyperspectral_Remote_Sensing_Scenes

Pavia University | Chikusei | DC Mall | Los Angeles 11 | Los Angeles 12 | Los Angeles 13 | Salinas | Cuprite

Figure 1. *Pseudocolor visualizations of the images under consideration.*

Table 1. Performance of FB-LRTA vs. LRTA for HS-MS Fusion

PSNR (dB)

Method	Pavia University	Chikusei	DC Mall	Los Angeles 11	Los Angeles 12	Los Angeles 13	Salinas	Cuprite
LRTA	42.70	40.49	50.64	41.75	51.80	44.14	48.90	53.88
FB-LRTA	43.05	41.13	57.02	50.22	57.25	50.24	52.78	56.66

Execution Time (sec)

LRTA	1.63	1.84	2.23	2.54	2.55	2.54	1.82	2.46
FB-LRTA	0.38	0.38	0.49	0.55	0.58	0.54	0.41	0.55

the University of Pavia in northern Italy. The original data has 610×610 pixels with 103 spectral bands over a spectral wavelength range of 430–860 nm with a 1.3-m spatial resolution; 93 spectral bands are preserved after removing water-absorption bands. The top-left $256 \times 256 \times 93$ subimage of dataset is adopted as the testing image.

The Chikusei image[4] was acquired over Chikusei, Ibaraki, Japan with a Headwall Hyperspec-VNIR-C airborne sensor. The original dataset has 128 bands over the 363–1018-nm range with 2517×2335 pixels at a 2.5-m spatial resolution. We use a $256 \times 256 \times 126$ subimage from the lower-right for testing, removing the last two spectral bands.

The DC Mall image[5] was acquired in 1995 over the National Mall in Washington, DC, using a Hyperspectral Digital Imagery Collection Experiment (HYDICE) sensor. A 256×256 spatial subimage is used, and the 210 spectral bands are reduced to 191 by eliminating water-absorption bands.

Finally, a number of images acquired using Airborne Visible/Infrared Imaging Spectrometer (AVIRIS) sensors are used. Our Los Angeles dataset is extracted from a large body of imagery available from NASA[6] and consists of radiance images acquired over several days in August 2013 above the city of Los Angeles, CA; the images are composed largely of dense urban scenery with 224 spectral bands over the range 400–2500 nm. Here, we use three images (Los Angeles 11, Los Angeles 12, and Los Angeles 13) for testing. Additionally, we also use the well-known Salinas and Cuprite AVIRIS images[7]. For all the AVIRIS images, a single 256×256 subimage (216×216 for Salinas) is extracted spatially from each image, and the available 224 AVIRIS spectral bands are reduced to 204 by removing water-absorption bands.

For all the results to follow, the spatial degradation operator $\mathbf{D}$ uses an 8×8 Gaussian point-spread kernel as in [7], while the spectral degradation operator $\mathbf{S}$ varies depending on the dataset. For Pavia University, an IKONOS-like spectral-response filter is used to generate a 4-band MSI consistent with [5, 7], while the DC Mall and AVIRIS datasets use a uniform spectral-response filter corresponding to Landsat TM bands 1–5 and 7 as in [3, 7]. The Chikusei image uses a similar Landsat-based uniform spectral filter corresponding to bands 1–4.

Table 1 presents the resulting experimental evaluations of PSNR as well as execution time. In Table 1, LRTA refers to Alg. 1 from [7] while FB-LRTA refers to Alg. 2 as proposed here. Note that LRTA was originally implemented in MATLAB on a CPU with no GPU acceleration in [7]. However, for the results here, LRTA has been reimplemented in PyTorch running on an RTX 3090 GPU. Likewise, the proposed FB-LRTA is also implemented in PyTorch on the same GPU. The results of Table 1 reveal a significant speedup for FB-LRTA; specifically, FB-LRTA is roughly 4 to 5 times faster than LRTA. This is due to FB-LRTA using one FB-SVT operation per iteration in contrast to the three SVT operations per iteration required by LRTA.

Interestingly—and perhaps contrary to intuition—even though the FB-SVT in FB-LRTA uses only an approximation to the left eigenvectors $\mathbf{U}$, this does not have a detrimental effect on the PSNR performance in HS-MS fusion. Indeed, Table 1 reveals that PSNR actually improves relative to LRTA; this gain in PSNR is particularly large for the DC Mall image as well as the three Los Angeles datasets. This appears to be due to the exclusive focus on spectral low-rankness that FB-LRTA implements by using only the mode-3 nuclear norm in (10). That is, the dense urban scenery in the DC Mall and Los Angeles images results in a relatively high spatial rank for these images that is ill-suited to the three-component norm (1) used by LRTA. On the other hand, while the Pavia University, Chikusei, Salinas, and Cuprite images also witness a gain in PSNR, it is less pronounced for these images, presumably due to the fact that they have smoother spatial features and thus relatively lower spatial rank.

[4] https://naotoyokoya.com/Download.html

[5] https://engineering.purdue.edu/~biehl/MultiSpec/hyperspectral.html

[6] https://popo.jpl.nasa.gov/mmgis-aviris/?s=ujooa

[7] http://www.ehu.eus/ccwintco/index.php?title=Hyperspectral_Remote_Sensing_Scenes

Conclusions

In this paper, we revisited the LRTA solution [7] to the HS-MS fusion problem, offering a pair of revisions to simplify and expedite processing. The resulting revised algorithm, FB-LRTA, featured two key revisions: whereas the original LRTA incorporated low-rank objectives both spatially and spectrally, FB-LRTA focused exclusively on spectral low-rankness. Additionally, the SVT—an SVD-driven operator used in LRTA to impose low-rankness—was replaced in FB-LRTA with a fixed-basis approximation (the FB-SVT) that eliminated the computationally costly SVD. These proposed modifications ultimately permitted the replacement of the three SVTs in LRTA in favor of one FB-SVT in FB-LRTA, resulting in significant runtime speedup. Additionally, empirical results for a number of images revealed improved image quality in the HS-MS fusion task for the proposed FB-LRTA in comparison to the original LRTA, despite the approximate nature of the underlying FB-SVT.

References

[1] N. Yokoya, C. Grohnfeldt, and J. Chanussot, "Hyperspectral and multispectral data fusion: A comparative review of the recent literature," *IEEE Geoscience and Remote Sensing Magazine*, vol. 5, no. 2, pp. 29–56, June 2017.

[2] M. Simões, J. Bioucas-Dias, L. B. Almeida, and J. Chanussot, "A convex formulation for hyperspectral image superresolution via subspace-based regularization," *IEEE Transactions on Geoscience and Remote Sensing*, vol. 53, no. 6, pp. 3373–3388, June 2015.

[3] N. Yokoya, T. Yairi, and A. Iwasaki, "Coupled nonnegative matrix factorization unmixing for hyperspectral and multispectral data fusion," *IEEE Transactions on Geoscience and Remote Sensing*, vol. 50, no. 2, pp. 528–537, February 2012.

[4] S. Li, R. Dian, L. Fang, and J. M. Bioucas-Dias, "Fusing hyperspectral and multispectral images via coupled sparse tensor factorization," *IEEE Transactions on Image Processing*, vol. 27, no. 8, pp. 4118–4130, August 2018.

[5] R. Dian and S. Li, "Hyperspectral image super-resolution via subspace-based low tensor multi-rank regularization," *IEEE Transactions on Image Processing*, vol. 28, no. 10, pp. 5135–5146, October 2019.

[6] S. Takeyama and S. Ono, "Robust hyperspectral image fusion with simultaneous guide image denoising via constrained convex optimization," *IEEE Transactions on Geoscience and Remote Sensing*, vol. 60, 2022.

[7] N. Liu, L. Li, W. Li, R. Tao, J. E. Fowler, and J. Chanussot, "Hyperspectral restoration and fusion with multispectral imagery via low-rank tensor-approximation," *IEEE Transactions on Geoscience and Remote Sensing*, vol. 59, no. 9, pp. 7817–7830, September 2021.

[8] K. Zhang, M. Wang, S. Yang, and L. Jiao, "Spatial-spectral-graph-regularized low-rank tensor decomposition for multispectral and hyperspectral image fusion," *IEEE Journal of Selected Topics in Applied Earth Observations and Remote Sensing*, vol. 11, no. 4, pp. 1030–1040, April 2018.

[9] T. Xu, T.-Z. Huang, L.-J. Deng, X.-L. Zhao, and J. Huang, "Hyperspectral image superresolution using unidirectional total variation with Tucker decomposition," *IEEE Journal of Selected Topics in Applied Earth Observations and Remote Sensing*, vol. 13, pp. 4381–4398, 2020.

[10] J.-F. Cai, E. Candès, and Z. Shen, "A singular value thresholding algorithm for matrix completion," *SIAM Journal on Optimization*, vol. 20, no. 4, pp. 1956–1982, 2010.

[11] J. Liu, P. Musialski, P. Wonka, and J. Ye, "Tensor completion for estimating missing values in visual data," *IEEE Transactions on Pattern Analysis and Machine Intelligence*, vol. 35, no. 1, pp. 208–220, January 2013.

[12] J. Yang and X. Yuan, "Linearized augmented Lagrangian and alternating direction methods for nuclear norm minimization," *Mathematics of Computation*, vol. 82, no. 281, pp. 301–329, January 2013.

[13] Z. Lin, R. Liu, and Z. Su, "Linearized alternating direction method with adaptive penalty for low-rank representation," in *Advances in Neural Information Processing Systems 24*, J. Shawe-Taylor, R. S. Zemel, P. L. Bartlett, F. Pereira, and K. Q. Weinberger, Eds., Granada, Spain, December 2011, pp. 612–620.

[14] W. Li, J. Liu, and Q. Du, "Sparse and low-rank graph for discriminant analysis of hyperspectral imagery," *IEEE Transactions on Geoscience and Remote Sensing*, vol. 54, no. 7, pp. 4094–4105, March 2016.

[15] Q. Du and J. E. Fowler, "Low-complexity principal component analysis for hyperspectral image compression," *International Journal of High Performance Computing Applications*, vol. 22, no. 4, pp. 438–448, November 2008.

[16] L. Wald, *Data Fusion: Definitions and Architectures*. Paris: Presses de l'École des Mines de Paris, 2002.

Author Biography

James E. Fowler *received the B.S. degree in computer and information science engineering and the M.S. and Ph.D. degrees in electrical engineering from The Ohio State University. He is currently a William L. Giles Distinguished Professor at Mississippi State University. He was previously Editor-in-Chief of IEEE Signal Processing Letters and was formerly Chair of the Computational Imaging Technical Committee of the IEEE Signal Processing Society. He is a Fellow of the IEEE.*

JOIN US AT THE NEXT EI!

electronic IMAGING

Imaging across applications . . . Where industry and academia meet!

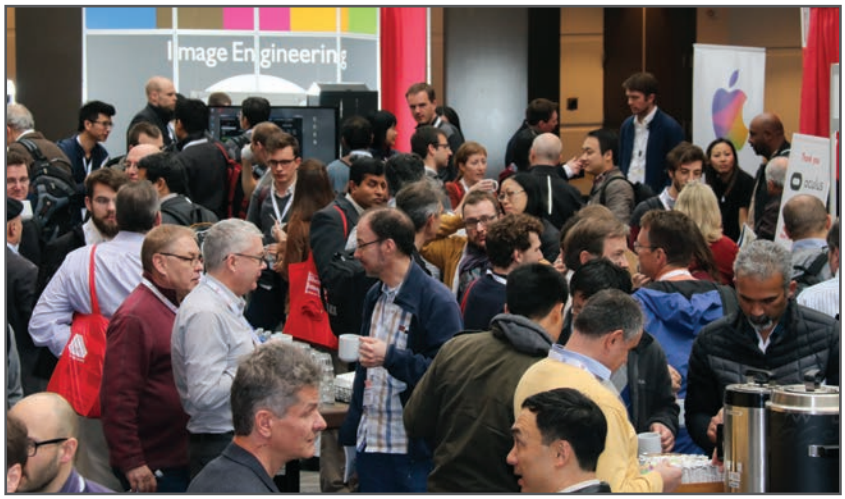

• SHORT COURSES • EXHIBITS • DEMONSTRATION SESSION • PLENARY TALKS •
• INTERACTIVE PAPER SESSION • SPECIAL EVENTS • TECHNICAL SESSIONS •

www.electronicimaging.org

ADVANCING IMAGING SCIENCE 75 1947 IS&T 2022 imaging.org